Department of Physics and Astronomy

Heidelberg University

Master thesis

in Physics

submitted by

Annika Oetjens

born in Bassum

2022

Planning and Testing

the Laser Beam Transfer Line

at CSR

This Master thesis has been carried out by Annika Oetjens

at the

Max Planck Institute for Nuclear Physics

under the supervision of

PD Dr. Holger Kreckel

Planen und Testen der Lasertransferstrecke am CSR

Mit dem Kryogenen Speicherring (CSR) am Max-Planck-Institut für Kernphysik in Heidelberg, ist es möglich innovative Forschung im Bereich der Atom- und Molekülphysik, wie auch der Astrophysik zu betreiben. Für die Durchführung von Experimenten im Bereich Spektroskopie, Ionen-Anregung oder Fragmentierung ist der Einsatz von Lasern erforderlich. Der bisherige Aufbau konnte keine idealen Bedingungen für die Durchführung von Laser-Experimenten bieten, sodass es in Bezug auf Laserleistung und Lasersicherheit zu Einschränkungen kam. In dieser Arbeit präsentiere ich die neue Lasertransferstrecke mit ihren Vorteilen, aber auch den Schwierigkeiten für eine optimierte Durchführung von Experimenten mit dem Einsatz von Lasern. Zu Beginn wurden die Laser in den angrenzenden Laserbereich versetzt. Einige der Laser divergieren sehr stark im freien Raum, sodass die größte Herausforderung der Intensitätsverlust über die Strecke zum CSR ist. Mit der Entwicklung einer Simulation zum Platzieren von optischen Elementen entlang des Strahlgangs, soll die zukünftige Umsetzung vereinfacht werden. Hierfür wurden Profile verschiedener Laser vermessen und die Parameter in die Simulation eingebunden. Abschließend wird der aktuelle Stand präsentiert und der reale Aufbau mit der Simulation verglichen.

Planning and Testing the Laser Beam Transfer Line at CSR

The Cryogenic Storage Ring (CSR) at the Max Planck Institute for Nuclear Physics in Heidelberg provides conditions for groundbreaking experiments in fundamental research in the fields of atomic and molecular physics, as well as astrophysics. For some of these experiments the application of lasers is necessary to perform spectroscopy, ion excitation or fragmentation. The previous setup did not provide ideal conditions for laser performance (stability, power output) nor laser safety. In this work I present design and construction of a new laser beam transfer line, and highlight its advantages but also the challenges arising from moving the lasers furthers away from CSR. Some of the lasers diverge greatly when propagating through free space. It is, therefore, a challenge to maximize the resulting laser power. To overcome this difficulty it was crucial to measure the different beam profiles and include these parameters in a simulation to describe laser beam propagation realistically. With this simulation the ideal position for optics can be found. Finally, the current status of the project is presented and the real setup compared to the simulation.

Contents

Acronyms

CCD Charge-Coupled Device

CSR Cryogenic Storage Ring

cw continuous wave

FWHM full width at half maximum

MCP Microchannel Plate

OPO Optical Parametric Oscillator

TEM_{00} fundamental mode

TEM_{mn} Transverse Electro-Magnetic wave

UV Ultraviolet

1 Introduction

The Cryogenic Storage Ring (CSR) at the Max Planck Institute for Nuclear Physics in Heidelberg is a next generation electro-static ion storage ring. With its nested vacuum structure and a closed liquid helium cycle, the ring can be cooled down to 3 K. The vacuum system provides number densities as low as 1000 cm^{-3} to 10 000 cm^{-3}, which correspond to a residual gas density of less than 10^{-14} mbar (at room temperature). Under these conditions, it is possible to store positive and negative atomic or molecular ions with kinetic energies of up to 300 keV per charge unit, almost independent of their mass. A sketch of the outline of CSR is shown in Figure 1.1

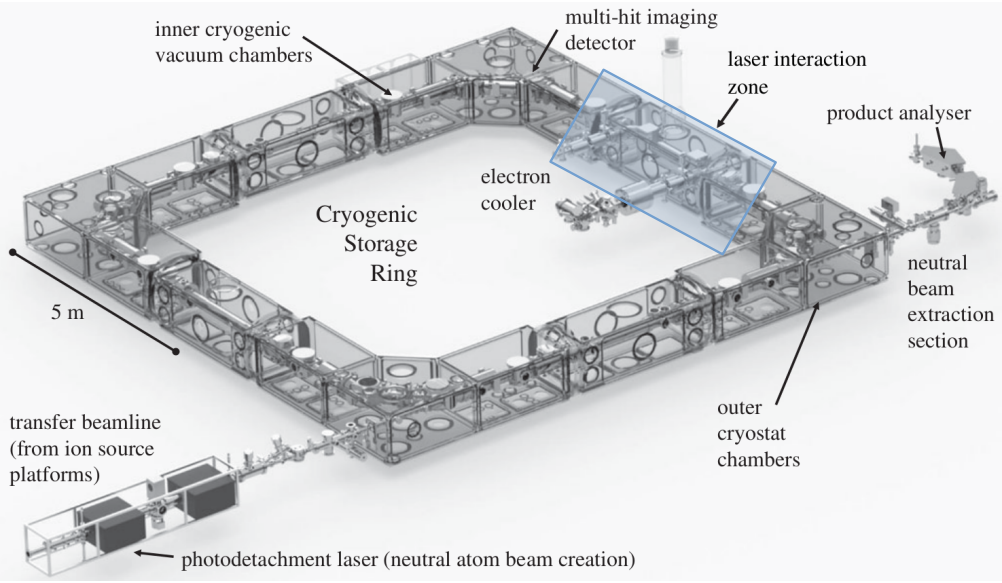

Figure 1.1: Outline of the Cryogenic Storage Ring (CSR) at the Max Planck Institute for Nuclear Physics with focus on the laser interaction region highlighted in blue, adapted from [1].

There are two high voltage platforms (300 keV and 60 keV) available to create

and then store both positive and negative ions. The ring has a circumference of 35.12 m in a fourfold symmetry, with dipole deflectors in each corner and focusing quadrupole doublets in the straight sections. The long storage times enable the study of slow processes which are relevant, e.g., in interstellar space.

Another feature of the CSR is an electron cooler, located in the same section as the laser interaction region. A collimated electron beam can be used for electron recombination and to reduce the phase space occupied by the particles by matching the velocites [2].

Two particle detectors are located right behind the electron cooling section. COMPACT ("COld Movable PArticle CounTer" [3, 4]) is a movable single-particle detector system for ions and neutralized atoms in the keV/u kinetic energy range based on Microchannel Plate (MCP) detection. NICE ("Neutral Imaging in Cold Environment" [5, 6]) functions also on the basis of MCP detection, but with a much larger active area and imaging capabilities.

Recently, Grussie et al. [7] introduced the ion-atomic merged beam setup (neutral beamline) at CSR to study atomic and molecular collisions. These are of interest in multiple areas of physics, for example astrophysics but also fundamental research and atmospheric chemistry. In laser experiments it was shown that infrared-active molecule ions cool to their lowest rotational states within storage time [8, 9].

Currently, a cryogenic reaction microscope ("CSR-REMI" [10]) is under construction, with the goal to observe individual reaction events of the stored molecular ions to learn more about their inner dynamics. An overview of CSR and the neighboring laser area is shown in Figure 1.2 and a more detailed review about CSR can be found in von Hahn et al. [11]. For the purpose of this work special focus is put on the region where the lasers are coupled into CSR and the photons interact with the ions (highlighted in blue).

1.1 Typical Applications

The following outlines a selection of past and future laser experiments to motivate the different features and demands the laser beam transfer line needs to satisfy.

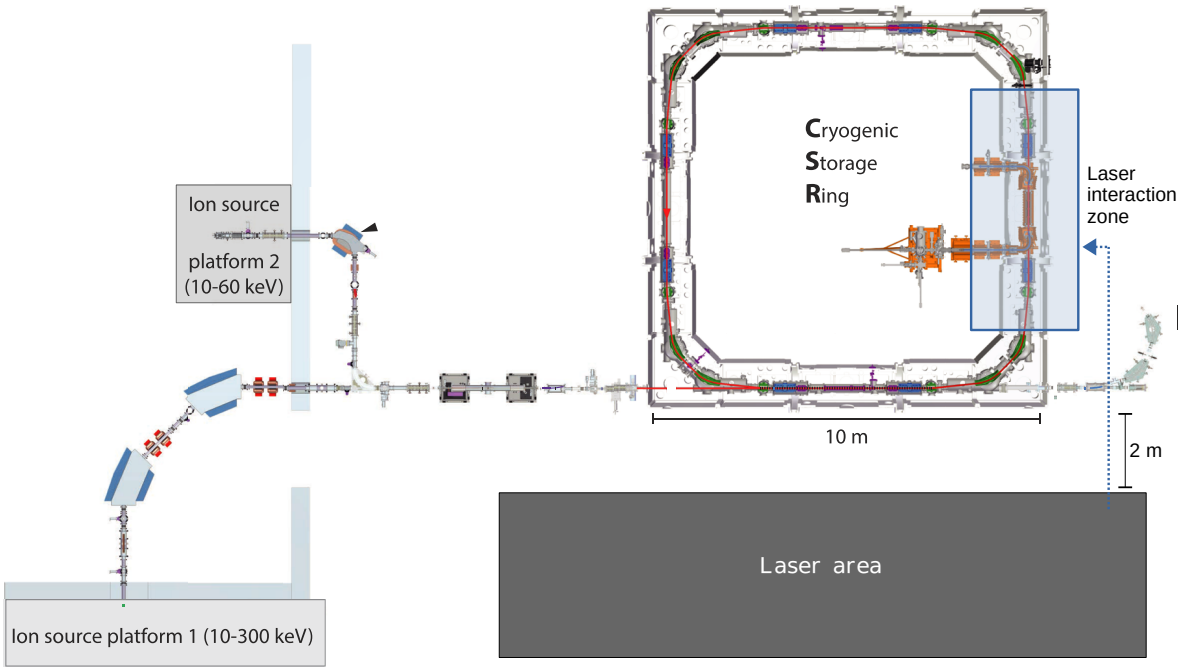

Figure 1.2: Detailled view of CSR with the newly build laser area next to the storage ring. The aim of this work is to construct a laser transfer bridge connecting the laser area with the entry ports of CSR in the laser interaction zone (blue dotted line), adapted from [7].

Photodetachment of Al_4^-

This experiment, performed by Müll et al. (in prep) was about delayed photodetachment of Al_4^- ions. A pulsed Optical Parametric Oscillator (OPO), which has a wide wavelength range of $220-2600\,\mathrm{nm}$, excites the ions to states slightly above the photodetachment threshold. The photon energy gets distributed statistically over all states in this energy region. Since this is only slightly above the photodetachment threshold, the ion stays in this internally excited state (order of $100\,\mu\mathrm{s}$) before the energy is transferred to the electron mode and the electron detaches. After this delayed photodetachment, the neutral particles are detected. To normalize the number of ions in the interaction region, a second laser is used. The photon energy of this continuous wave (cw) laser is much higher and leads to instant photodetachment, thus providing a value for normalizing the absolute ion number. For longer storage times the lower energy states get more and more depleted so that higher photon

energies are required to get the molecule in the range of delayed photodetachment. This emphasizes the versatility of a tunable, high energy pulsed laser (with mediocre beam quality) and legitimates the time and effort going into setting up the optical elements.

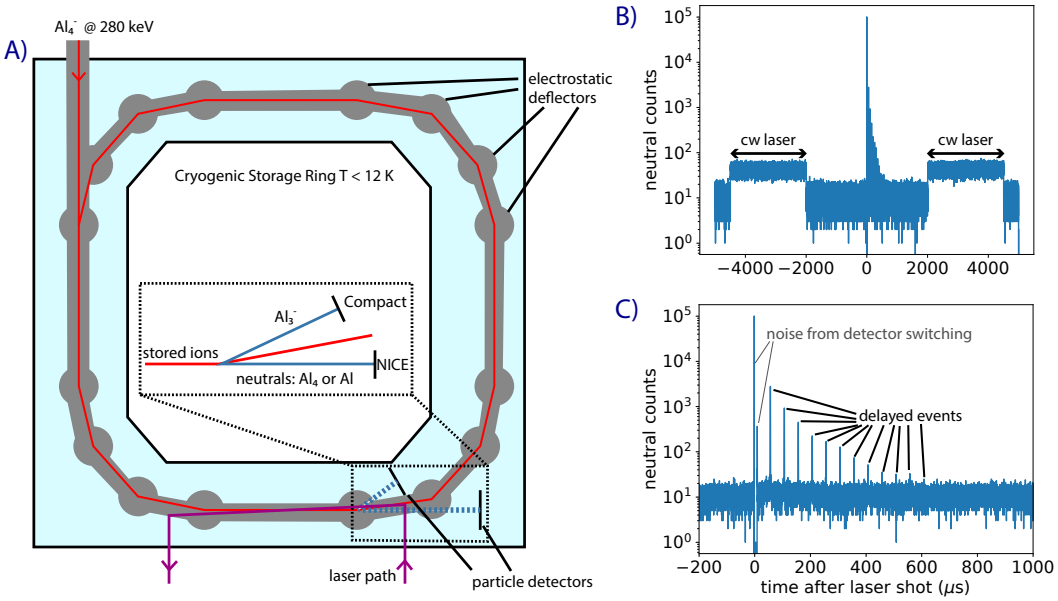

Figure 1.3: Setup of the Al_4^- measurement with two lasers (Müll et al in prep).

In Figure 1.3 the experimental setup is shown. The scientific analysis is still ongoing, but the realization of the experiment reveals some of the demands and challenges in this area of research. The requirement to use lasers with different wavelengths simultaneously and have a stable output over multiple hours is demanding. In addition, the optical setup needed adjusting in between some of the runs, requiring an evacuation of the whole area to ensure laser safety. For future setups it is desirable to improve on laser stability, access to the optical elements and laser safety .

Metastable states of Si^-

Si^- is one of a few atomic anions with several metastable states. During this experiment, Si^- was stored with a kinetic energy of 58 keV. To learn more about the decay of metastable states, selective photodetachment was employed. The study, published by Müll et al. [12], set up a complicated measurement procedure to get results for the metastable lifetimes. A schematic of the laser setup is shown in Figure 1.4. The measurement of this system was extremely difficult, one complication

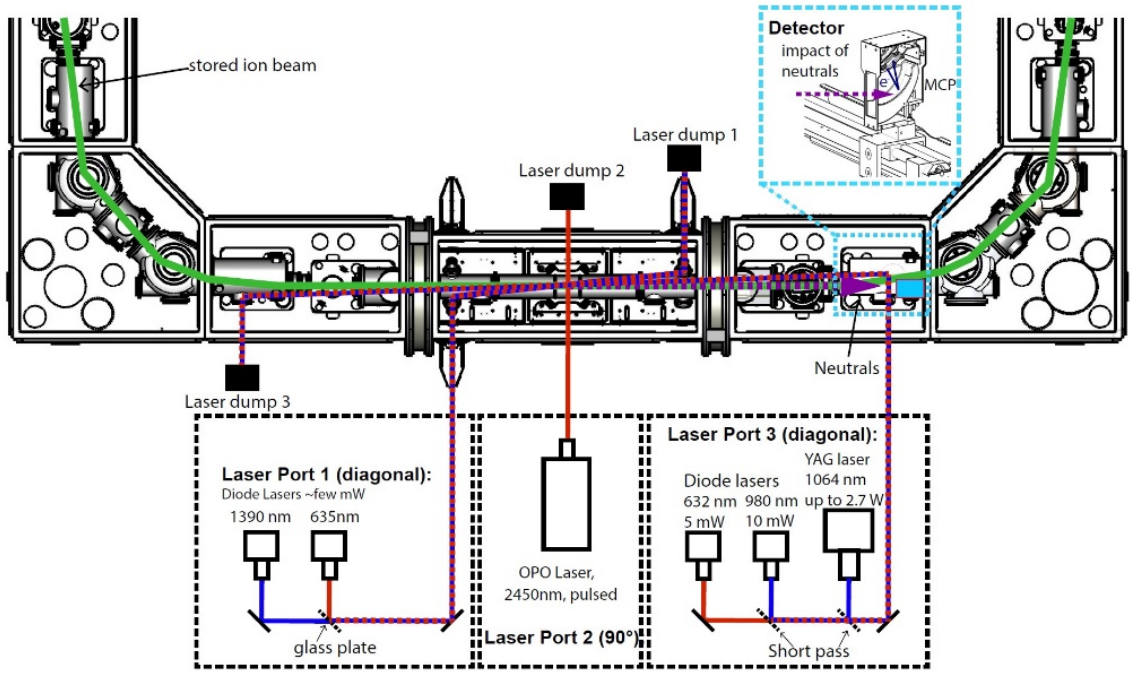

Figure 1.4: Experimental setup to measure the long lived metastable states of Si^- [12]

being that a lot of laser power was lost due to the different entry ports and due to alignment issues. Scientifically, this was interesting since the studied lifetimes of the anionic states with little background perturbations are found in agreement with theoretical computations. The CSR provides the environment to probe states that used to be inaccessible in the past and versatile laser setups with a reliable power output are essential.

Highly excited states of H_3^+

Znotins et al. [13] present an experiment to reach the highly excited states of H_3^+. Being the most simple polyatomic molecule it plays an important role in understanding interstellar ion-neutral chemistry. Exploring the range close to the dissociation limit would strengthen its role as a benchmark system for theoretical computations. A direct vertical transition to states above $20\,000\,\mathrm{cm}^{-1}$ has a prohibitively small signal strength so that it is proposed to use a three step scheme. In this measurement scheme, H_3^+ is stored in a storage ring. Three different photon energies are needed to get from the ground state to the first and second transition state and then finally via UV radiation in the pre-dissociation regime (Figure 1.5). Performing this multi-step

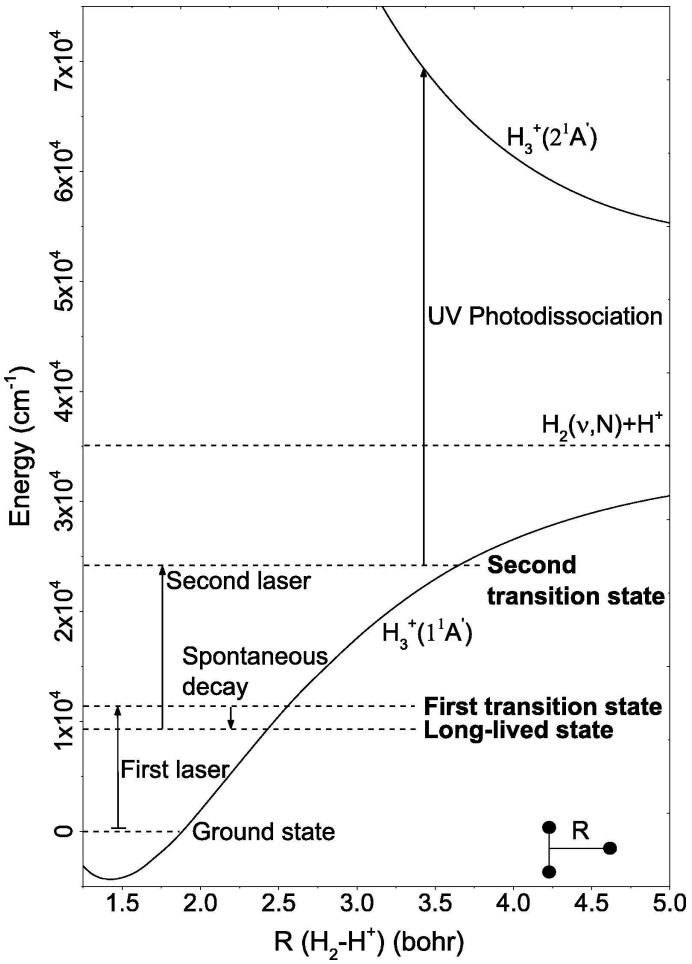

Figure 1.5: Measurement scheme for H_3^+ [13]

excitation procedure would be challenging in itself, where three lasers are needed simultaneously, thus, highlighting the importance of having a setup where the laser output is as high and as stable as possible.

1.2 Motivation

In the previous experiments the lasers were placed right next to the entry ports of CSR. This has of course the advantage of a relatively short beam path. However, there are numerous disadvantages that make it worthwhile thinking about developing an improved setup. First off, there are lasers whose output power is susceptible to temperature. The experimental hall itself is not temperature controlled and influenced by the ambient climate. Additionally, the lasers, although placed in

boxes, are exposed to dust and dirt, which is also impacting their lifetimes. Figure 1.6 shows the arrangement where it is not only cramped and the lasers are exposed to vibrations, but also laser safety is an issue. For changes to the optical setup inside the laser boxes it is necessary to close off the whole area around CSR, making it laborious to perform any adaptations.

In this work I present the laser beam transfer line as an upgrade to improve the performance and the results of laser experiments at CSR.

The laser beam transfer line with the design, its features and the final setup is presented in Chapter 2 and an overview of the theory behind laser beam propagation is outlined in Chapter 3. Chapter 4 demonstrates the beam profile measurements and the following Chapter 5 presents the laser simulation and the results. To improve beam stability a laser beam stabilization system is tested in Chapter 6. Chapter 7 presents the final installation and a first test before the conclusion and outlook are given in Chapter 8.

Figure 1.6: Showing the previous laser positioning (black boxes) right next to CSR (June 2021).

2 Laser Beam Transfer Line

2.1 Demands and Features

The new beamline needs to support experimental setups like the ones performed in the past but also help improve any possible configuration in the future (Chapter 1). The most important parts are the laser stability and laser safety. Therefore, the lasers have been moved into a new laser area next to CSR. Here, they are in a temperature controlled, air filtered environment. Shielded from the rest of the experimental hall this simplifies matters with regards to laser safety. An addition to this is the fully enclosed beam path with the possibility to guide several parallel beams to the entry ports while leaving all CSR viewports still accessible for future alterations. Since some of the lasers have a greatly diverging beam profile, it is necessary to provide space to install lenses and diagnostics to refocus the beam. This was solved by having six aluminum chambers with a blackboard base along the path. One of the chambers is also wider to allow for the placement of mirrors to overcome misalignment issues. Also, it is possible to open this specific chamber towards the neutral beamline, which might be of use in the future. An additional feature is that the whole beamline can be evacuated by a roughing pump to the mbar regime. This reduces scattering, air turbulences and absorption and is analyzed more closely in Section 2.2. The entire beamline covers a distance of around 20 m and has to be 3 m above ground to keep escape routes free. This motivates the second part of this work. To reduce time needed to align and install lenses in this inconvenient height, a laser beam propagation simulation (Chapter 5) helps to find the right placement beforehand. Figure 2.1 shows the bridge and highlights some of the features, as it was designed in collaboration with the construction department.

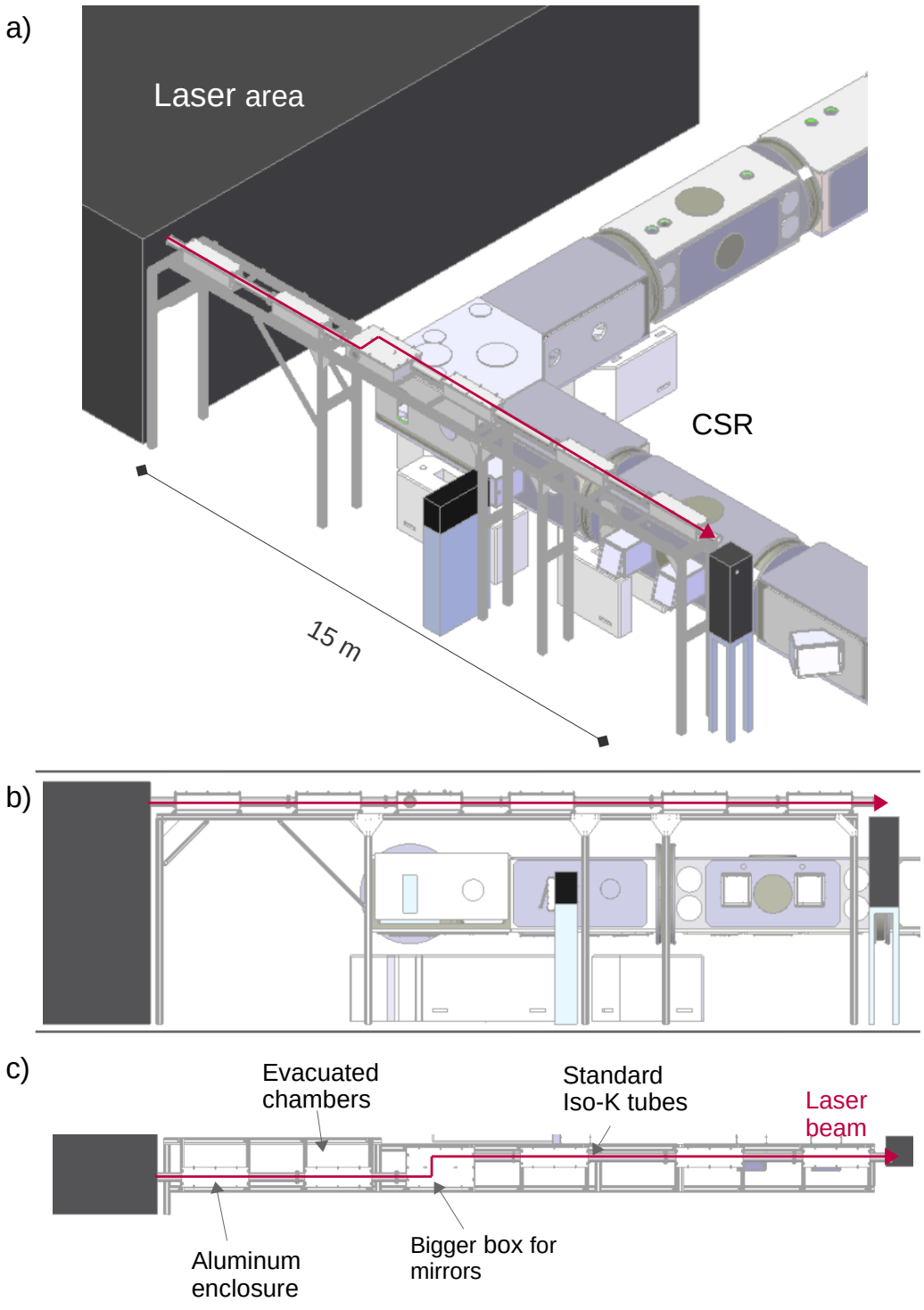

Figure 2.1: Schematic drawing of the laser beam transfer line at CSR, a) Isometric view, b) Side view and c) Top view.

2.2 UV Absorption by Water Vapor

In various discussions about the biggest challenges in transporting the laser beam along the path, losses due to absorption in air were mentioned. One factor in particular was the absorption due to water vapor concerning the Ultraviolet (UV) wavelength region. How big of an impact this really has, is evaluated below. In Pei et al. [14] the cross section σ of water vapor absorption in the UV is experimentally determined to be:

$$\sigma \sim 10^{-24}\ \mathrm{cm}^2/\mathrm{molecule} \tag{2.1}$$

According to the Lambert-Beer law [15], the flux decays exponentially depending on the cross-section σ, the number density n and the distance z.

$$\Phi \sim \exp\left(-\sigma \cdot \mathrm{n} \cdot z\right) \tag{2.2}$$

The number density is a function of partial water vapor pressure $\mathrm{P_v}$, Boltzmann constant k_B and temperature T:

$$\mathrm{n} = \frac{\mathrm{P_v}}{k_B \mathrm{T}} \tag{2.3}$$

The water vapor pressure itself is a function of the temperature dependent saturation pressure $\mathrm{P_{sat}}$ [16] and the given humidity $\mathcal{H} \in [0,1]$.

$$\mathrm{P_v(T)} = \mathcal{H} \cdot \mathrm{P_{sat}(T)}\ ,\ \mathcal{H} \in [0,1] \tag{2.4}$$

$$\mathrm{P_{sat}(T)} = 0.61078 \cdot \exp\left(\frac{17.27 \cdot \mathrm{T}}{\mathrm{T} + 237.3}\right) \tag{2.5}$$

For typical values of 15 °C to 30 °C, as one can also see in Figure 2.2, this results in:

$$\mathrm{P_{sat}}(15°\mathrm{C}) = 1706\ \mathrm{Pa} \qquad \mathrm{n}(15°\mathrm{C}) = 8.2 \cdot 10^{24}\ \mathrm{m}^{-3}$$
$$\mathrm{P_{sat}}(30°\mathrm{C}) = 4246\ \mathrm{Pa} \qquad \mathrm{n}(30°\mathrm{C}) = 10.2 \cdot 10^{24}\ \mathrm{m}^{-3}$$

Inserting these values in Equation 2.2 gives an upper limit (for T = 30 °C and $\mathcal{H} = 100\%$) for a 30 m beam path of a flux reduction of less than 2%. The impact of

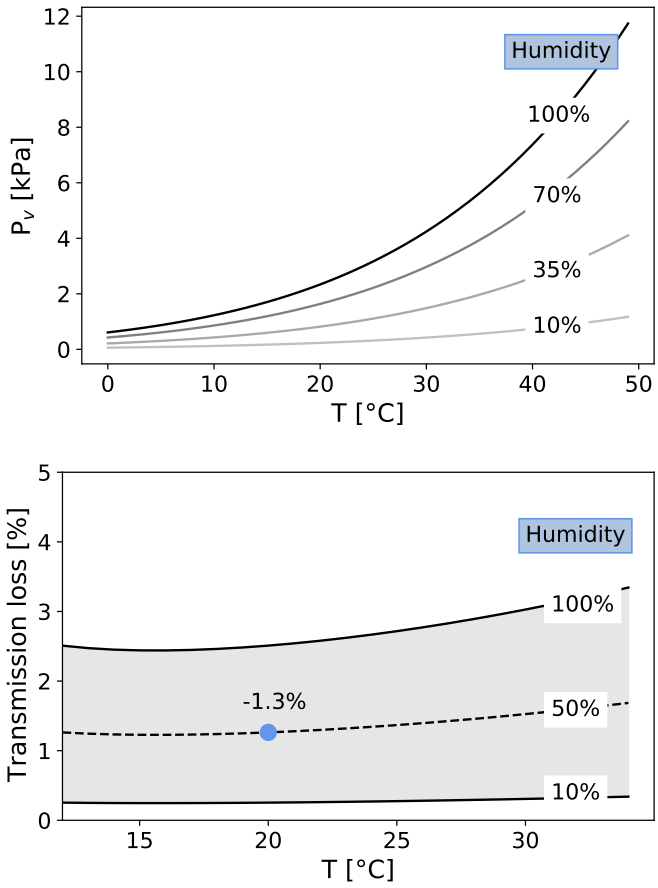

Figure 2.2: Top: Humidity (10% - 100%) and temperature dependent curves for the water vapor pressure P_v as computed above. Bottom: Relative flux loss over a propagation distance of 30 m for different temperatures and humidity. The blue dot indicates the normal room conditions leading to a transmission loss of 1.3%.

UV absorption due to water vapor is, thus, not as significant as expected. However, it is still benefiting for beam stability to evacuate the chambers and exclude or reduce any negative impact, e.g., air turbulences. Adding to this is that the beamline is supposed to serve all possible future setups as well, one of which might be in the mid-Infrared wavelength region. So, it still seems beneficial to include the possibility to evacuate the path.

3 Light Amplification by Stimulated Emission Radiation

The basic principle of the functioning of a laser is the population inversion in a multi-level system. In the following I present the simple case of a 3-level system as it was used in, e.g., [17]. Electrons from the ground state E_1 are excited, e.g., by collisions or a flash light, to a higher lying state E_3. E_3 is an unstable state so that the electron will rapidly decay to a lower lying state E_2. Once, from this meta-stable state photons with a specific frequency given by the energy difference $\omega_{21} = (E_2 - E_1)/\hbar$ are emitted, this triggers more electrons to decay and emit photons with this specific frequency and spatial direction. This process is called stimulated emission and is the relevant process to emit laser light as seen in Figure 3.1. Lasing is possible as long as the population of N_2 is bigger than N_1.

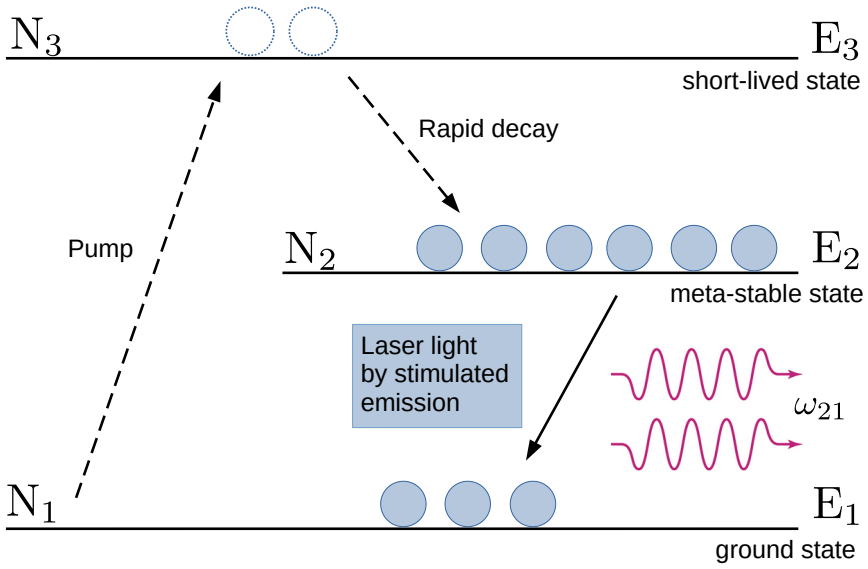

Figure 3.1: Schematic of the principle of population inversion by stimulated emission.

3.1 Gaussian Beam Propagation

The following derivations are adapted from [18], [19], [20] and [21]. The propagation of a laser beam can be described by a Transverse Electro-Magnetic wave (TEM_{mn}). The subscripts m and n refer to the different radial and angular modes. Starting with the Maxwell equations in matter with $\mathbf{E}$ the electric field, electric charge density ρ, electric current $\mathbf{J}$ and $\mathbf{B}$ the magnetic field (letters in bold represent vectors):

$$\nabla \times \mathbf{E} = -\frac{\partial \mathbf{B}}{\partial \mathrm{t}} \qquad \nabla \cdot \mathbf{D} = \rho \tag{3.1}$$

$$\nabla \times \mathbf{H} = \mathbf{J} + \frac{\partial \mathbf{D}}{\partial \mathrm{t}} \qquad \nabla \cdot \mathbf{B} = 0 \tag{3.2}$$

The displacement field $\mathbf{D}$ and the magnetizing field $\mathbf{H}$ are related to the electric and magnetic field via the permittivity ϵ and permeability μ:

$$\mathbf{D} = \epsilon \mathbf{E} + \mathbf{P} \qquad \text{with polarization } \mathbf{P} \tag{3.3}$$

$$\mathbf{H} = \frac{1}{\mu}\mathbf{B} - \mathbf{M} \qquad \text{with magnetization } \mathbf{M} \tag{3.4}$$

Assuming a homogeneous, isotropic, non conducting, source-free, dielectric medium the Maxwell equations simplify to:

$$\nabla \times \mathbf{E} = -\frac{\partial \mathbf{B}}{\partial \mathrm{t}} \qquad \nabla \cdot \mathbf{E} = 0 \tag{3.5}$$

$$\nabla \times \mathbf{B} = \mu\epsilon \cdot \frac{\partial \mathbf{E}}{\partial \mathrm{t}} \qquad \nabla \cdot \mathbf{B} = 0 \tag{3.6}$$

Applying the curl operator to Equation 3.5 and inserting Equation 3.6, the magnetic field $\mathbf{B}$ can be eliminated:

$$\nabla \times (\nabla \times \mathbf{E}) = \nabla \times \left(\frac{-\partial \mathbf{B}}{\partial \mathrm{t}} \right) \tag{3.7}$$

$$= -\frac{\partial}{\partial \mathrm{t}} (\nabla \times \mathbf{B}) \tag{3.8}$$

$$= -\mu\epsilon \cdot \frac{\partial^2 \mathbf{E}}{\partial \mathrm{t}^2} \tag{3.9}$$

Making use of the vector identity $\nabla \times \nabla \times \mathbf{E} = \nabla^2 \mathbf{E}$, the wave equation is deduced:

$$\nabla^2 \mathbf{E} = \mu\epsilon \cdot \frac{\partial^2 \mathbf{E}}{\partial \mathrm{t}^2} \tag{3.10}$$

The wave equation is solved by plane waves which can be separated into their time and space dependence, or an envelope and a carrier wave ($\mathbf{r} = (\mathrm{x,y,z})^\intercal$).

$$\mathbf{E}(\mathbf{r}, t) = \mathbf{E}_0 \cdot e^{i(\omega t - \mathbf{kr})} \rightarrow \mathbf{E}(\mathbf{r}, t) = \mathbf{E}(\mathbf{r}) \cdot e^{i\omega t} \tag{3.11}$$

Inserting Equation 3.11 into the wave equation 3.10:

$$\nabla^2 \mathbf{E}(\mathbf{r}) \cdot e^{i\omega t} = -\omega^2 \mu\epsilon \cdot \mathbf{E}(\mathbf{r}) \cdot e^{i\omega t} \tag{3.12}$$

and using $\mathbf{k}^2 = \omega^2 \mu\epsilon$ this simplifies to the Helmholtz equation:

$$\left(\nabla^2 + \mathbf{k}^2\right) \cdot \mathbf{E}(\mathbf{r}) = 0 \tag{3.13}$$

For the application to a laser beam the paraxial approximation (propagation along the optical axis $\mathbf{z} = z \cdot \vec{e}_z$) takes hold, so that divergence effects are minimal in the near field.

$$\mathbf{E}(x, y, z) = \psi(x, y, z) \cdot e^{-i\mathbf{kz}} \tag{3.14}$$

Also, it is reasonable to assume that $\psi(x, y, z)$ is a slowly varying function describing the transverse intensity distribution, inserting it into the Helmholtz equation:

$$\nabla^2 \mathbf{E}(x, y, z) = \left(\nabla^2 \psi - 2i\mathbf{kz} \cdot \nabla\psi\right) e^{-i\mathbf{kz}} = -k^2 \psi \cdot e^{-i\mathbf{kz}} \tag{3.15}$$

Rearranging leads to

$$\nabla^2 \psi - 2i\mathbf{k}\frac{\partial \psi}{\partial z} = 0 \tag{3.16}$$

using

$$\left|\frac{\partial^2 \psi}{\partial z^2}\right| \ll 2k \left|\frac{\partial \psi}{\partial z}\right| \tag{3.17}$$

leads to the paraxial wave equation:

$$\frac{\partial^2 \psi}{\partial x^2} + \frac{\partial^2 \psi}{\partial y^2} - 2ik\frac{\partial \psi}{\partial z} = 0 \tag{3.18}$$

The paraboloidal wave E(r) $\sim (1/r) \cdot e^{-ikr}$ is an exact solution to the paraxial wave equation, and using the paraxial approximation ($x^2 + y^2 \ll z^2$) this can be written as a Gaussian:

$$E(r) = \psi(r) \cdot e^{-ikz} = \frac{E_0}{z} \exp\left[-ikz\left(1 + \frac{x^2+y^2}{2z^2}\right)\right] \tag{3.19}$$

with r $= \sqrt{x^2+y^2+z^2} = z\sqrt{1+\frac{x^2+y^2}{z^2}}$.

Being an exact solution Equation 3.19 must therefore be independent of the origin. Shifting the function by any number ξ (this can also be imaginary) must still be a solution.

Since the shift ξ can also be part imaginary a complex beam parameter q can be introduced (with z_R being a real number):

$$q = z - \xi = z + iz_R \tag{3.20}$$

The complex parameter q can be split into a real and an imaginary part:

$$\frac{1}{q} = \frac{1}{q_R} - i\frac{1}{q_i} \tag{3.21}$$

The origin itself can also be shifted by $-\xi$ and plugging this into Equation 3.19 leads to:

$$\psi(x,y,z) = \frac{E_0}{q(z)} \exp\left[\frac{-ik(x^2+y^2)}{2}\frac{1}{q(z)}\right] \tag{3.22}$$

The reason for introducing the complex parameter $q(z)$ is that it allows for formulating simple propagation laws. The origin is defined as the position where the beam radius has a minimum, called the beam waist $\omega(z=0) = \omega_0$, and the radius of curvature is infinite $R(z=0) = \infty$.

$$\frac{1}{q} = \frac{1}{R(z)} - i\frac{\lambda}{\pi\omega^2(z)} \tag{3.23}$$

$$\frac{1}{q_0} = -i \cdot \frac{\lambda}{\pi\omega_0^2} \tag{3.24}$$

$$q_0 = i \cdot \frac{\pi\omega_0^2}{\lambda} = i \cdot r_R \tag{3.25}$$

This defines the Rayleigh range r_R, the length scale over which the beam spreads due to diffraction. For the beam radius this means that it has increased by a factor $\sqrt{2} \cdot \omega_0$. In general, the beam radius is defined in relation to the full width at half maximum (FWHM) of the intensity distribution:

$$\omega(z) = \frac{FWHM(z)}{\sqrt{2 \cdot \ln 2}} \tag{3.26}$$

The phase shift which the beam experiences during the propagation is called the Gouy phase shift and can also be expressed in terms of the Rayleigh range. The following gives an overview of all the relevant parameters to characterize Gaussian beam propagation.

Beam width	$\omega(z) = \omega_0 \left[1 + \left(\frac{z}{z_R}\right)^2\right]^{1/2}$	(3.27)
Radius of curvature	$\mathrm{R(z)} = z \left[1 + \left(\frac{z}{z_R}\right)^2\right]$	(3.28)
Rayleigh length	$z_R = \frac{\pi\omega_0^2}{\lambda}$	(3.29)
Divergence angle	$\theta = \frac{\omega}{z} = \frac{\lambda}{\pi\omega_0}$	(3.30)
Gouy phase shift	$\phi = \arctan\left(z/z_R\right)$	(3.31)

See also Figure 3.2 for an overview of the parameters.

The solution to the paraxial wave equation given above is called the fundamental mode ($\mathrm{TEM_{00}}$). The general solution to the wave equation includes all possible resonator modes in transverse and longitudinal direction. In the application of laser systems it is, however, desirable to get the smallest, most collimated spot size and,

therefore have resonators favoring the fundamental mode.

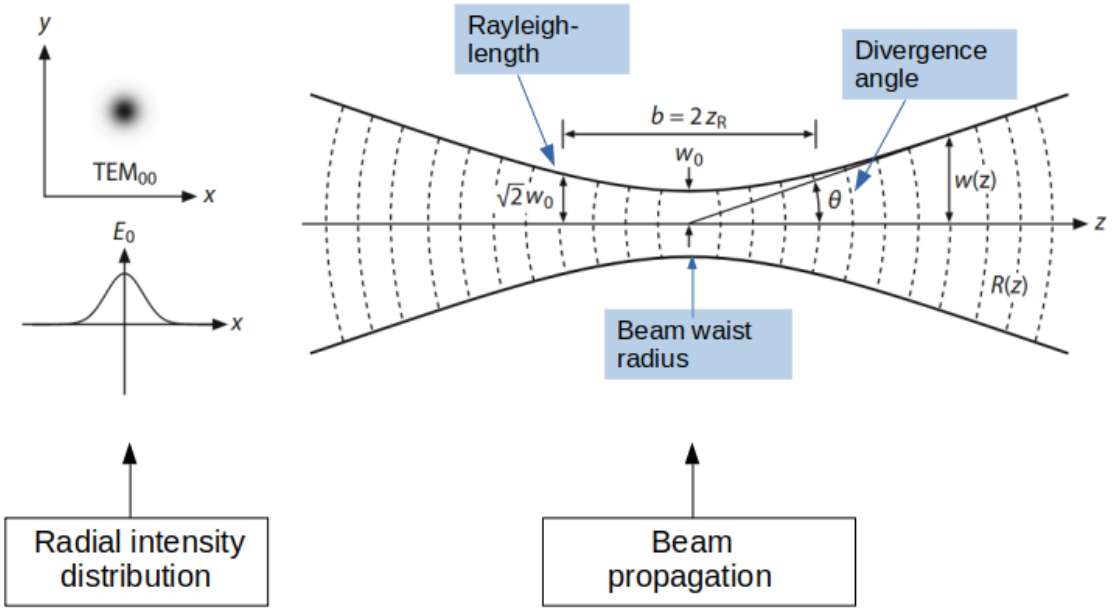

Figure 3.2: Gaussian beam characteristics, adapted from [18].

3.2 Beam Propagation Using the ABCD Matrix Analysis

In the previous section the relevant parameters to characterize a laser beam were formulated. In this section it is derived how these parameters, mainly beam radius, Rayleigh length and divergence angle, change when covering a certain distance (free space propagation) or when passing through a lens. The goal is to make use of the ABCD matrix analysis, in mathematics called the ray transfer matrix analysis, to describe the beam radius and divergence along the beam path and compute the influence of passing through lenses. This theory simplifies the propagation to a 2D vector-matrix multiplication.

Again, using the paraxial approximation, it is assumed that the beam experiences only small deviations from the optical axis. This also ensures the small angle approximation ($\sin\theta \approx \theta$).

With this assumption the ingoing beam parameters, i.e. beam waist ω_0 and divergence angle θ, can be related to the outgoing ones:

$$\begin{bmatrix} \omega_0' \\ \theta' \end{bmatrix} = \begin{bmatrix} A & B \\ C & D \end{bmatrix} \cdot \begin{bmatrix} \omega_0 \\ \theta \end{bmatrix} \tag{3.32}$$

The ABCD matrix is representing the optical system the beam passes through and the four entries are given by:

$$A = \omega_0'/\omega_0 \qquad B = \omega_0'/\theta \tag{3.33}$$

$$C = \theta'/\omega_0 \qquad D = \theta'/\theta \tag{3.34}$$

The representation for free space (air, distance d) and a thin lens (focal length f) are given by:

$$\text{Free space} \qquad \begin{bmatrix} A & B \\ C & D \end{bmatrix} = \begin{bmatrix} 1 & \mathrm{d} \\ 0 & 1 \end{bmatrix} \tag{3.35}$$

$$\text{Thin lens} \qquad \begin{bmatrix} A & B \\ C & D \end{bmatrix} = \begin{bmatrix} 1 & 0 \\ -1/\mathrm{f} & 1 \end{bmatrix} \tag{3.36}$$

For a beam path consisting of a combination of lenses and free space in between, the matrices for the different components are multiplied:

$$\begin{bmatrix} \omega_0' \\ \theta' \end{bmatrix} = \begin{bmatrix} A & B \\ C & D \end{bmatrix}_n \cdot \ldots \cdot \begin{bmatrix} A & B \\ C & D \end{bmatrix}_1 \cdot \begin{bmatrix} A & B \\ C & D \end{bmatrix}_0 \cdot \begin{bmatrix} \omega_0 \\ \theta \end{bmatrix} \tag{3.37}$$

Hence, the beam radius can be determined at every point along the path as depicted in Figure 3.3.

As seen in Section 3.1 the beam radius can be deduced from the complex parameter $q(z)$, Equation 3.23. So the beam propagation can also be formulated in terms of $q(z)$:

$$q' = \frac{Aq + B}{Cq + D} \tag{3.38}$$

After travelling a distance d the propagation leads to:

$$q' = q + d \tag{3.39}$$

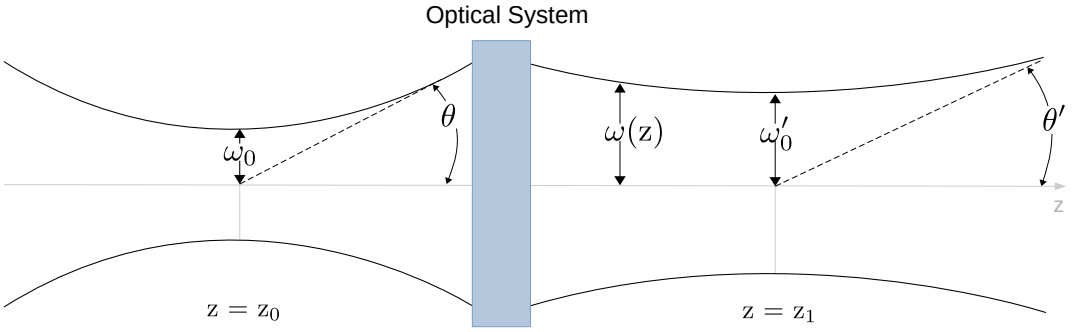

Figure 3.3: Beam propagation through an optical system.

Meaning both the beam radius $\omega(z)$ and the radius of curvature R(z) increase after propagating in free space.

When passing through a lens, the complex parameter transforms to:

$$q' = \frac{q}{-\frac{q}{f} + 1} \tag{3.40}$$

So that the beam size is unchanged and only the curvature is affected.

3.3 Real Lasers: M² Beam Propagation Factor

The theory of Gaussian beams is a good starting point to describe the laser beam propagation. However, a real laser beam does differ from the idealized Gaussian beam. In reality it simply is often not possible to create laser cavities that solely output the fundamental mode TEM_{00}. This gives rise to mode mixtures which affect the way the beam radius and divergence change during propagation. Some of these modes are shown in Figure 3.4. This means that simulating a real beam with an

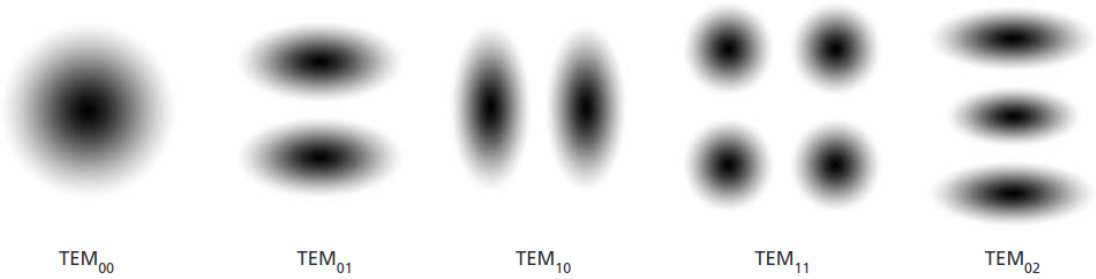

Figure 3.4: Example of a few higher order Hermite-Gaussian modes that can contribute to the resulting laser beam [21].

ideal Gaussian beam leads to deviations. To overcome this issue the propagation laws need to be adapted. The method commonly used is to introduce an extra parameter that characterizes the differences between real and ideal Gaussian beam propagation, denoted as M^2 [20, 21]. M^2 is a measure of how much the real beam differs from the ideal diffraction-limited Gaussian beam.

For the evolution of the beam radius this results in:

$$\omega^2(z) = \omega_0^2 \left[1 + \left(M^2 \cdot \frac{z}{z_R} \right)^2 \right] \tag{3.41}$$

For the complex beam parameter $q(z)$ holds:

$$\frac{1}{q} = \frac{1}{R} - i \cdot \frac{M^2 \lambda}{\pi r^2} \tag{3.42}$$

This can then be used for the ABCD matrix computation. For an ideal Gaussian beam $M^2 = 1$ and the original equations can be retrieved. Figure 3.5 shows a visualization of adopting the propagation factor to accommodate for the difference between a real and ideal laser beam.

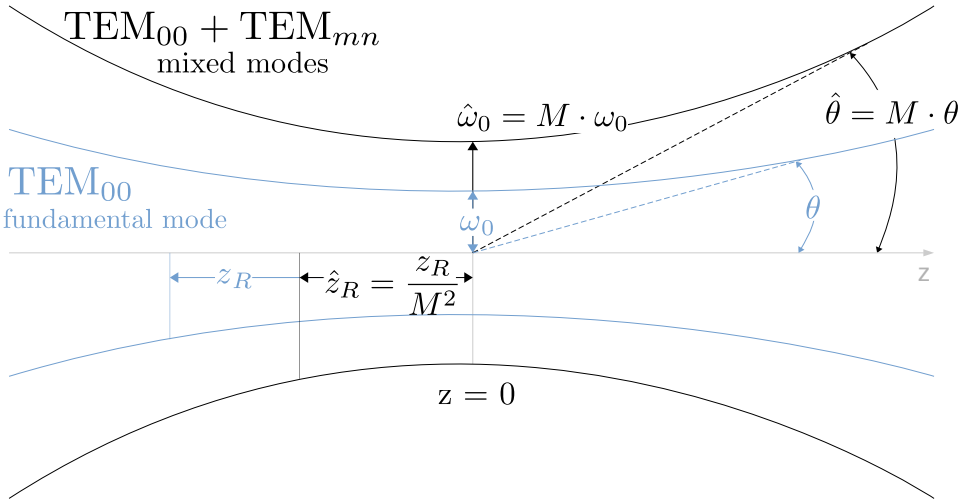

Figure 3.5: The propagation of a laser beam along the optical axis z. In blue the ideal Gaussian beam consisting simply of the fundamental mode TEM_{00}. In comparison, the real laser beam (black) is a mixture of modes and the beam parameter (beam waist ω_0 and divergence angle θ differ from the ideal by a factor M.

To experimentally determine the M^2 factor multiple measurements of the beam radius along the propagation axis need to be made. Since the value is also a quality factor for the given laser, it is desirable to have a standardized procedure. The ISO norm 11146 [22] provides this standard. For our measurement we made use of a commercially available measurement system that also allows us to measure the other beam parameters.

4 Beam Profile Measurement

To perform realistic simulations of different laser beams, it is essential to obtain the respective laser profile. For this purpose a M^2-measurement device and a Charge-Coupled Device (CCD) camera from Thorlabs were purchased. In the following the setup and the results from the measurement with different lasers are presented. The device comes with a designated software. To obtain a realistic value for M^2 it is necessary to perform the following steps:

1. Beam alignment: To avoid distortion, the laser has to enter the system without angular offset, when adding the focusing lens.

2. Intensity: Since the CCD camera is highly sensitive, saturation has to be avoided.

3. Meaurement: The beam profile is measured around the vicinity of the beam waist. To fulfill the ISO-norm, at least ten measurement steps have to be taken. From these ten steps five have to be within the Rayleigh length, and five outside of it. The beam radius can then be fitted in a parabolic fit, Figure 4.1, from which the parameters such as divergence and Rayleigh length are derived.

Figure 4.2 shows the M^2-measurement system. In red, the incoming beam which is guided through a focusing lens, hits two mirrors on a translation stage which can vary the length of the beam path before it then enters the beam profiler, a CCD camera.

We test the system with three different lasers which are shown on the right in Figure 4.2.

- OBIS 637 [23]
  The single-frequency cw diode laser at 637 nm is specified to output the fundamental mode TEM_{00} with a low $M^2 \leq 1.2$.

- CTL 950 [24]
  The continuously tunable (910 nm to 980 nm) diode laser is operated at 945 nm. It is also specified to output the fundamental mode, a M^2 value is not provided.

- OPO [25]
  This optical parametric oscillator is widely tunable (220 nm to 2600 nm) and pulsed at 20 Hz. The profile is specified as "Hat-top" in the near field.

Results

Only for one of the three lasers a factory value for M^2 was provided. This makes it difficult to validate the measurement results, which are shown in Figure 4.3). For the OBIS a value of $M^2 = 1.7$ was acquired. This is a little higher than the factory value of $M^2 = 1.2$ but from experience these values are often lower than the actual ones so this is acceptable. For the CTL we actually measured the lowest M^2 value of only 1.2, which will be great to work with. The OPO was the most interesting one since the profile is very much not Gaussian but has somewhat of a cross shape. But since this laser is one of the most important one for experiments we are very interested in obtaining a value to make optical alignment easier. For the OPO we determined the beam propagation factor to be $M^2 = 30$.

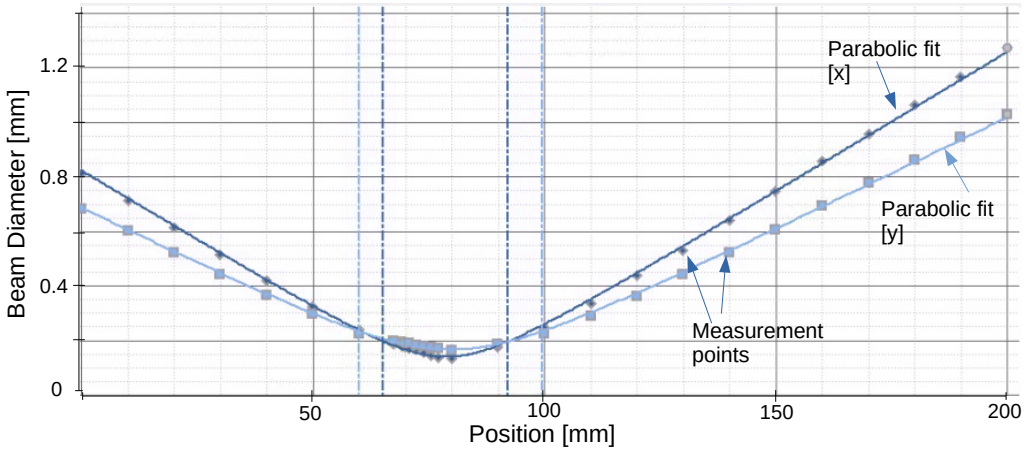

Figure 4.1: Performing a fit to the measurement points in the vicinity of the beam waist.

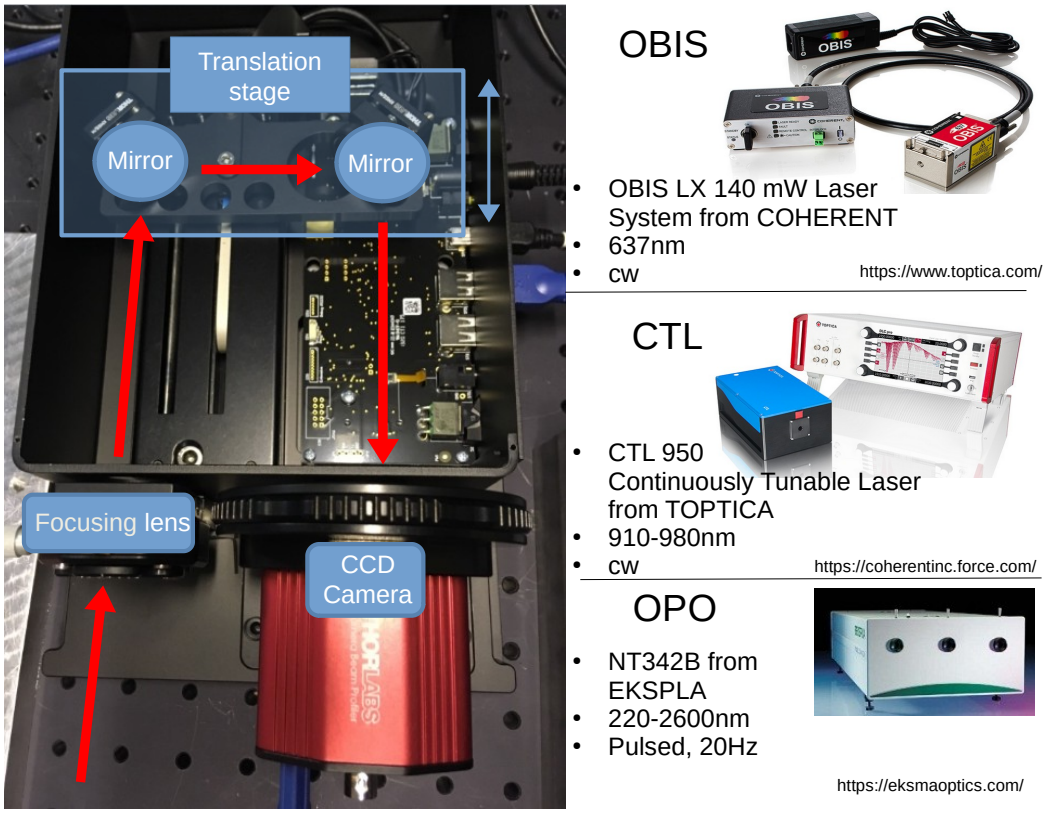

Figure 4.2: Left: The M^2- measurement device from Thorlabs. Right: Overview of the different lasers.

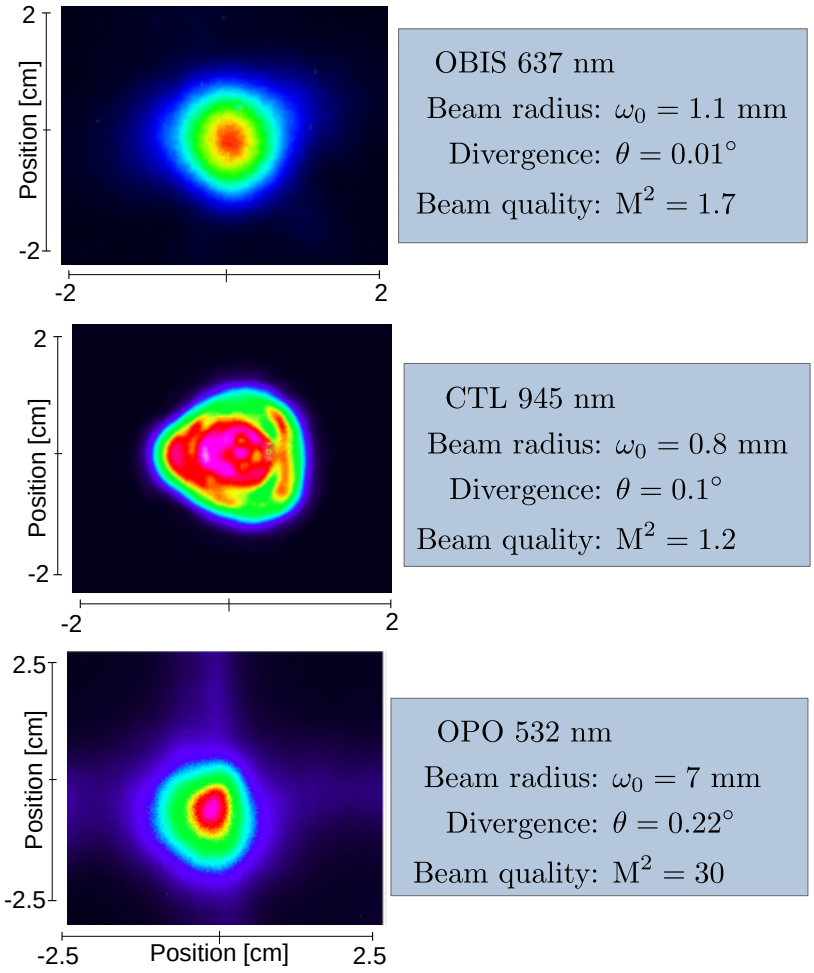

Figure 4.3: Overview of the different laser profiles and their beam parameter.

5 Laser Simulation

The aim of a realistic laser simulation is to improve and simplify the setup of optics to guide the laser beam along the designated path. The main focus is to increase the resulting laser output that arrives at the experiment. The assumption that a laser beam can be approximated as a Gaussian beam is only valid to a certain extent, and the more accurately the laser profile can be characterized, the more applicable the simulation. In the previous Chapter 4 beam profiler measurements were presented. In combination with the laser propagation theory and M^2 factor from Chapter 3, a realistic simulation of beam propagation can now be realized.

In the following there is a short overview of the code I developed followed by the results for three different lasers.

5.1 Code Setup

I developed the program in Python3 [26] and it is available on my Github [27] account. The main script calls the functions needed for ABCD matrix propagation, the text file specifying the lenses (focal length and position) and the input file providing the beam characteristics. The latter two are the only ones that need adapting in order to find the most suitable optical setup. In this case the fixed parameters are the total length and the position of the boxes along the bridge. A sketch of the code's structure is shown in Figure 5.1

5.2 Simulation Results

Recalling the laser beam parameter from Table 5.2, measured in Chapter 4, we can now make use of the simulation and try different lens positions to find the optimal setup.

To get as much as possible of the laser power to the experiment, the beam cannot exceed the size of the optical elements. In our setup we use 1" (25 mm) diameter mirrors and lenses. The goal is to use as few lenses as possible since every lens

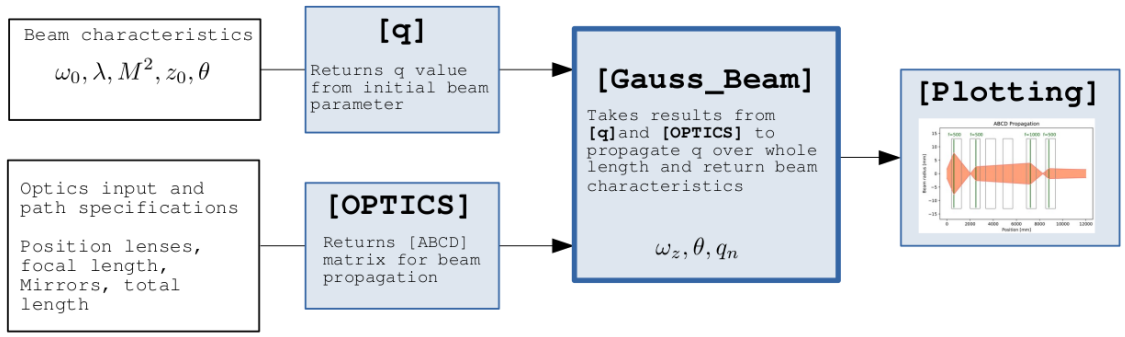

Figure 5.1: Setup of the python program to compute the beam propagation of a Gaussian like laser profile including the propagation factor. The two white boxes on the left represent the two input files. The blue boxes are the different functions that perform the propagation. A more detailed description can be found in Section 5.1.

decreases the flux and demands decent alignment to avoid distortion. For the OBIS and CTL, both diode lasers, this is fairly uncritical, they behave almost Gaussian (the CTL with $M^2 = 1.2$ close to perfect Gaussian). For these two it would be enough to focus the beam with two lenses, in this example with focal lengths f = 200, in one of the chambers on the bridge. For the OPO, on the other hand, this is more demanding. The beam deviates greatly ($M^2 = 30$) from a Gaussian and with an initial beam waist of 7 mm this needs a lot more focusing to reach the end of the beamline. In the test at a wavelength of 532 nm we would need early focusing while still being on the laser table. Due to the large divergence angle, here, four lenses (all f = 500) are needed on the bridge. To align all the lenses becomes increasingly more difficult the more lenses are involved. That was the main reason to have one of the chambers (third from the left) bigger so that one can redirect the beam with the help of mirrors. For more details and images refer to Chapter 2. The results are presented in Figure 5.2 along with a sketch of the beamline. The size of the grey

Parameter	OBIS	CTL	OPO
Wavelength [nm]	637	945	532
Type	cw	cw	pulsed 20Hz
Beam waist radius ω_0 [mm]	1.1	0.8	7
Divergence θ	0.01°	0.1°	0.22°
Propagation factor M^2	1.7	1.2	30

Table 5.1: Summary: Beam parameter for the different lasers.

boxes, indicating the position of the chambers, is also the size of the mirrors and lenses to indicate the maximum beam radius before being cut off.

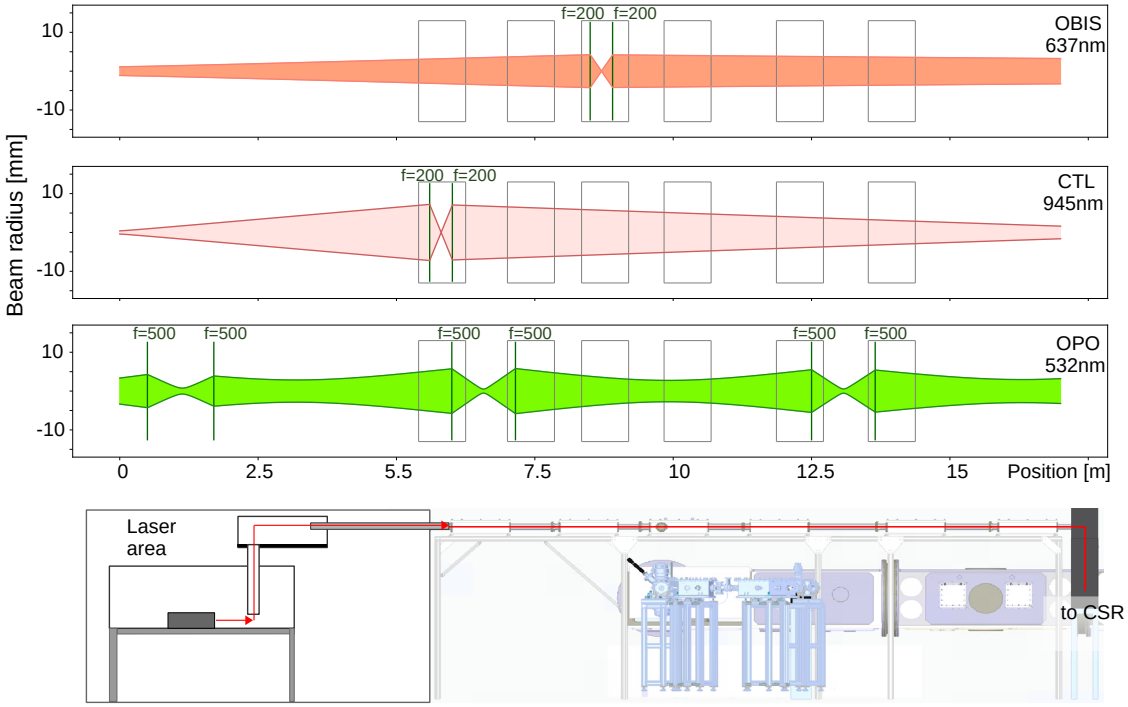

Figure 5.2: Beam propagation simulation for the three different lasers. Green vertical lines indicate the position of lenses and focal length f, the grey boxes the position of the aluminum boxes along the bridge. On the bottom is a sketch of the actual setup; to the left the laser table in the laser area and to the right the bridge guiding the beam to the CSR entry port. For the OPO additional lenses already on the laser table are needed to guide the beam successfully.

6 Laser Beam Stabilization System

A previous attempt to transfer the OPO laser beam from a laser hut to the experiment failed and was eventually build back. So this time we did not want to take any chances.

Besides the careful construction and implementation of various chambers for alignment additional support is added: An active laser beam stabilization system made by a local company in Heidelberg [28]. The idea is to place two piezo actuators in the beam path and have the corresponding detectors measure the variation in the beam's position. Over a distance of over 20 m a small angular change might lead to a massive loss in power, which we want to avoid. To gauge the system's potential we performed multiple tests. The biggest challenge was the 20 Hz pulsed OPO, as the stabilization system was not designed for this kind of pulse frequency and the company was not sure if it would even work.

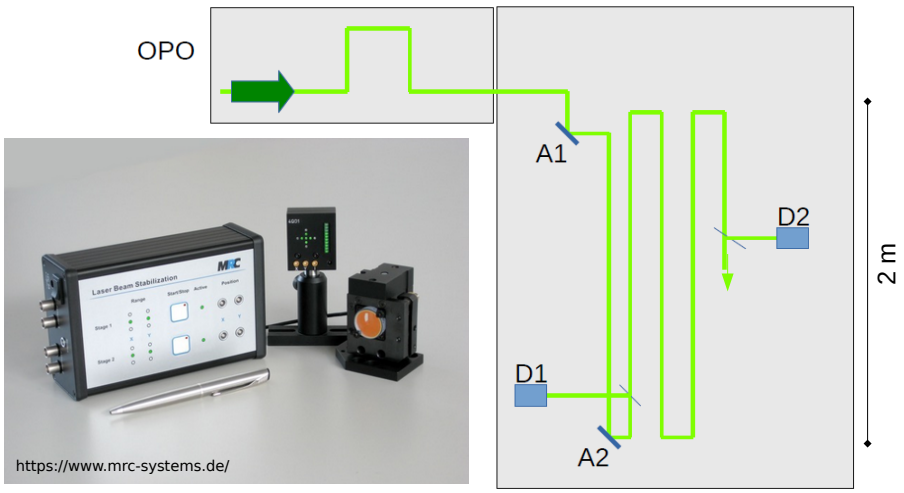

Figure 6.1: Left: Picture of the stabilization system. Right: Setup for testing the OPO, over a distance of roughly 12 m. A1, A2 indicate the positions of the actuators and D1, D2 the two corresponding detectors.

The OPO does not only have a beam profile that is far from the ideal Gaussian but the beam also exits the laser box at different angles depending on the wavelength. In past measurements switching between wavelengths had lead to readjustments of mirrors which will only be amplified by the increased distance.

To get a realistic idea of how much power is lost simply by the divergence, we set up a path of roughly 12 m and include the two actuators and detectors from the active beam stabilization system, i.e. see Figure 6.1. After getting used to the system we start by making a series of measurements storing the beam's position on the detectors.

The results are documented in Figure 6.2. The lighter blue shows the beam's behavior when the stabilization system is turned off. The different symbols represent different wavelengths. So even for one wavelength the beam jumps back and forth on a scale of 60 µm. Switching between wavelengths leads to significant angular differences, explaining the difficulties with losing laser power during wavelength scans in past experiments. When the system is turned on, all wavelengths are focused in the center. There is still some spread but since the system was not designed for pulsed lasers of only 20 Hz this result is quite encouraging.

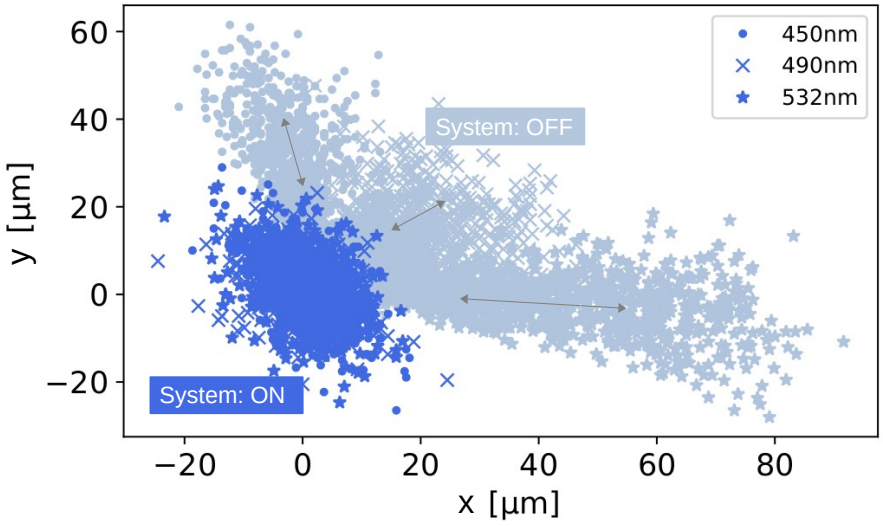

Figure 6.2: Time-resolved beam positions on detector for different wavelengths (450 nm, 490 nm, 532 nm). System off: Light blue, beam moves back and forth (grey arrows) and changes angles for different wavelengths. System on: Dark blue, beam is centered for all wavelengths over time.

In conclusion, the system does work with the OPO and it will be of great use when transferring the beam. The OPO was definitely a worst case scenario for the system, so that it should stabilize other laser beams much better.

7 First Light

To conclude this work, it is the goal to test the finished laser beam transfer line with a laser and see how well it works. The OBIS can be operated at 0.5 mW and is, therefore, ideal for a first alignment. The biggest challenge was to get the beam from the laser table to the height of the bridge. Without any lenses the beam diverges as expected but can be spotted at the end of the line. The finished bridge and the beam path from inside the laser area are shown in Figure 7.1.

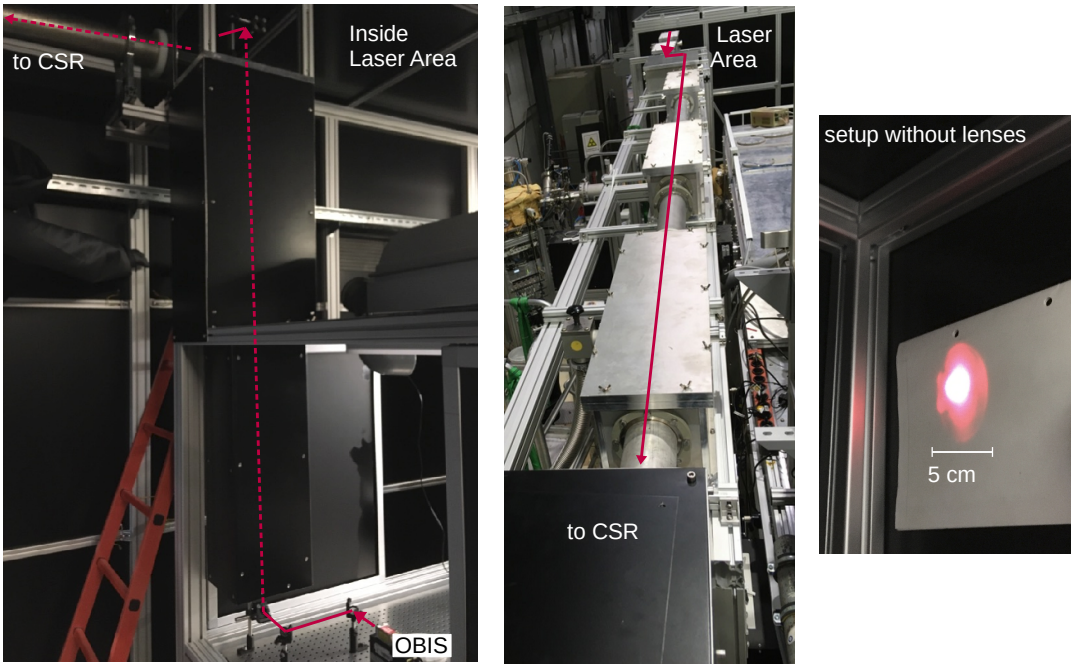

Figure 7.1: Testing the laser beam transfer line with the OBIS 637 nm diode laser. Left: beam path from the laser table up to the entry to the transfer line. Center: View towards to laser area, showing all the chambers, to the right is CSR. Right: Beam at the end of the transfer line, first setup without lenses (July 2022).

Comparison to the simulation

The next step is to introduce lenses. With the simulation we know the position to be in the bigger chamber and get an estimate of where to place them. Here, we want to refocus the beam with a telescope of two lenses with focal lengths of 200 mm. Whenever possible it is advised to use this bigger chamber for lenses since it also has enough space to have mirrors following the lenses to realign the beam and hit the center of the tube.

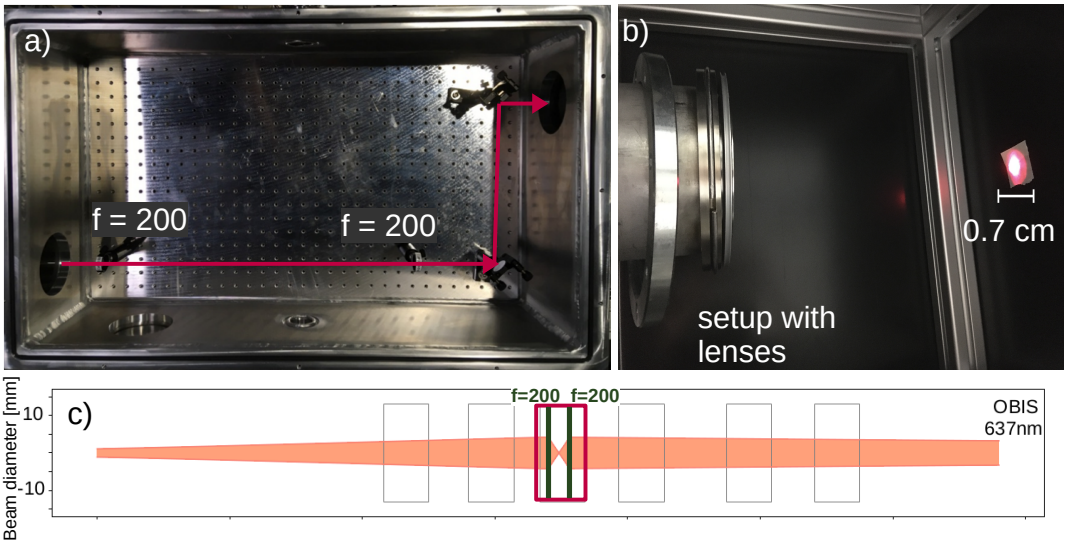

Figure 7.2: a) Optical setup in the bigger chamber, b) OBIS spot size at the end of the transfer line, and c) comparison to the simulation, highlighting the respective chamber.

The simulation is a realistic display of how to focus the beam, which is also shown in Figure 7.2. To conclude this analysis we also compared the flux loss to what we would expect. Every mirror and lens contributes to flux reduction and if everything is well aligned the loss should not exceed the inevitable loss from the optical elements.

For this setup we used silver coated mirrors which reflect an estimated amount of 97% for this wavelength. The plano-convex calcium fluoride lenses have a transmission of roughly 93%. In total the setup consists of seven mirrors and the two lenses, resulting in a flux loss of roughly 30%:

$$\Phi = \Phi_0 \cdot (0.97^7 \cdot 0.93^2) \tag{7.1}$$

$$= \Phi_0 \cdot 0.7 \tag{7.2}$$

We take a power measurement before the first mirror (0.56 mW) and one measurement at the end of the beamline (0.38 mW). So that for this setup we have a loss of 33% coming real close to the estimate above. Since the losses for the mirrors and lenses are also just estimates we can expect that most of the flux is actually lost on the optics and not cut off.

8 Conclusion and Outlook

In this work I presented the process of designing and testing the laser beam transfer line at CSR. This new setup will enhance the realization of laser experiments in the future by highlighting the importance of laser performance and safety. By making use of the Gaussian beam propagation and ABCD matrix analysis, possible optical setups along the bridge can be determined beforehand. Measuring the different beam profiles and introducing the beam propagation factor M^2 made the simulation more realistic. Luckily, the bridge was finished just before the end of this project so that it was possible to perform first tests and have light at the end of the tunnel. With this the project is successfully concluded!

In the future, different settings for the different lasers have to be thoroughly tested and it will be a challenge to transport all the necessary beam power to the experiment. When using the propagation simulation one has to keep in mind the influence of mirrors and lenses which can distort the beam when not perfectly aligned. The implementation of the laser stabilization system and motorized mirror holders will help to perform beam alignment without having to open up the chambers or climbing up the ladders every time.

A Lists

A.1 List of Figures

A.2 List of Tables

B Bibliography

[1] H. Kreckel, O. Novotný, and A. Wolf. Astrochemical studies at the Cryogenic Storage Ring. *Philosophical Transactions of the Royal Society of London Series A*, 377(2154):20180412, September 2019. doi: 10.1098/rsta.2018.0412.

[2] Oldřich Novotný, Patrick Wilhelm, Daniel Paul, Ábel Kálosi, Sunny Saurabh, Arno Becker, Klaus Blaum, Sebastian George, Jürgen Göck, Manfred Grieser, Florian Grussie, Robert von Hahn, Claude Krantz, Holger Kreckel, Christian Meyer, Preeti M. Mishra, Damian Muell, Felix Nuesslein, Dmitry A. Orlov, Marius Rimmler, Viviane C. Schmidt, Andrey Shornikov, Aleksandr S. Terekhov, Stephen Vogel, Daniel Zajfman, and Andreas Wolf. Quantum-state-selective electron recombination studies suggest enhanced abundance of primordial HeH^+. *Science*, 365(6454):676–679, August 2019. doi: 10.1126/science.aax5921.

[3] Kaija Spruck, Arno Becker, Florian Fellenberger, Manfred Grieser, Robert von Hahn, Vincent Klinkhamer, Oldřich Novotný, Stefan Schippers, Stephen Vogel, Andreas Wolf, and Claude Krantz. An efficient, movable single-particle detector for use in cryogenic ultra-high vacuum environments. *Review of Scientific Instruments*, 86(2):023303, February 2015. doi: 10.1063/1.4907352.

[4] C. Krantz, O. Novotný, A. Becker, S. George, M. Grieser, R. von Hahn, C. Meyer, S. Schippers, K. Spruck, S. Vogel, and A. Wolf. Single-particle detection of products from atomic and molecular reactions in a cryogenic ion storage ring. *Nuclear Instruments and Methods in Physics Research A*, 851: 92–102, April 2017. doi: 10.1016/j.nima.2017.01.050.

[5] X. Urbain, D. Bech, J. P. Van Roy, M. Géléoc, S. J. Weber, A. Huetz, and Y. J. Picard. A zero dead-time multi-particle time and position sensitive detector based on correlation between brightness and amplitude. *Review of Scientific Instruments*, 86(2):023305, February 2015. doi: 10.1063/1.4908597.

[6] A. Becker. *Imaging of Neutral Fragmentation Products from Fast Molecular Ion Beams: Paving the Way for Reaction Studies in Cryogenic Environment*. PhD thesis, Ruprecht-Karls-Universität Heidelberg, 2016.

[7] F. Grussie, A. P. O'Connor, M. Grieser, D. Müll, A. Znotins, X. Urbain, and H. Kreckel. An ion-atom merged beams setup at the Cryogenic Storage Ring. *Review of Scientific Instruments*, 93(5):053305, May 2022. doi: 10.1063/5.0086391.

[8] C. Meyer, A. Becker, K. Blaum, C. Breitenfeldt, S. George, J. Göck, M. Grieser, F. Grussie, E. A. Guerin, R. von Hahn, P. Herwig, C. Krantz, H. Kreckel, J. Lion, S. Lohmann, P. M. Mishra, O. Novotný, A. P. O'Connor, R. Repnow, S. Saurabh, D. Schwalm, L. Schweikhard, K. Spruck, S. Sunil Kumar, S. Vogel, and A. Wolf. Radiative Rotational Lifetimes and State-Resolved Relative Detachment Cross Sections from Photodetachment Thermometry of Molecular Anions in a Cryogenic Storage Ring. *Physical Review Letters*, 119(2):023202, July 2017. doi: 10.1103/PhysRevLett.119.023202.

[9] A. P. O'Connor, A. Becker, K. Blaum, C. Breitenfeldt, S. George, J. Göck, M. Grieser, F. Grussie, E. A. Guerin, R. von Hahn, U. Hechtfischer, P. Herwig, J. Karthein, C. Krantz, H. Kreckel, S. Lohmann, C. Meyer, P. M. Mishra, O. Novotný, R. Repnow, S. Saurabh, D. Schwalm, K. Spruck, S. Sunil Kumar, S. Vogel, and A. Wolf. Photodissociation of an Internally Cold Beam of CH^+ Ions in a Cryogenic Storage Ring. *Physical Review Letters*, 116(11):113002, March 2016. doi: 10.1103/PhysRevLett.116.113002.

[10] F. Schotsch, I. Zebergs, S. Augustin, H. Lindenblatt, L. Hoibl, D. Djendjur, C. D. Schroeter, T. Pfeifer, and R. Moshammer. TrapREMI: A reaction microscope inside an electrostatic ion beam trap. *Review of Scientific Instruments*, 92(12):123201, December 2021. doi: 10.1063/5.0065454.

[11] R. von Hahn, A. Becker, F. Berg, K. Blaum, C. Breitenfeldt, H. Fadil, F. Fellenberger, M. Froese, S. George, J. Göck, M. Grieser, F. Grussie, E. A. Guerin, O. Heber, P. Herwig, J. Karthein, C. Krantz, H. Kreckel, M. Lange, F. Laux, S. Lohmann, S. Menk, C. Meyer, P. M. Mishra, O. Novotný, A. P. O'Connor, D. A. Orlov, M. L. Rappaport, R. Repnow, S. Saurabh, S. Schippers, C. D. Schröter, D. Schwalm, L. Schweikhard, T. Sieber, A. Shornikov, K. Spruck,

S. Sunil Kumar, J. Ullrich, X. Urbain, S. Vogel, P. Wilhelm, A. Wolf, and D. Zajfman. The cryogenic storage ring CSR. *Review of Scientific Instruments*, 87(6):063115, June 2016. doi: 10.1063/1.4953888.

[12] D. Müll, F. Grussie, K. Blaum, S. George, J. Göck, M. Grieser, R. von Hahn, Z. Harman, Á. Kálosi, C. H. Keitel, C. Krantz, C. Lyu, O. Novotný, F. Nuesslein, D. Paul, V. C. Schmidt, S. Singh, S. Sunil Kumar, X. Urbain, A. Wolf, and H. Kreckel. Metastable states of Si^- observed in a cryogenic storage ring. *Phys. Rev. A*, 104:032811, Sep 2021. doi: 10.1103/PhysRevA.104.032811. URL `https://link.aps.org/doi/10.1103/PhysRevA.104.032811`.

[13] Aigars Znotins, Florian Grussie, Andreas Wolf, Xavier Urbain, and Holger Kreckel. An approach for multi-color action spectroscopy of highly excited states of H_3^+. *Journal of Molecular Spectroscopy*, 378:111476, April 2021. doi: 10.1016/j.jms.2021.111476.

[14] Linsen Pei, Qilong Min, Yuyi Du, Zhechen Wang, Bangsheng Yin, Kai Yang, Patrick Disterhoft, Thomas Pongetti, and Lei Zhu. Water Vapor Near-UV Absorption: Laboratory Spectrum, Field Evidence, and Atmospheric Impacts. *Journal of Geophysical Research: Atmospheres*, 124(24):14310–14324, 2019. doi: https://doi.org/10.1029/2019JD030724. URL `https://agupubs.onlinelibrary.wiley.com/doi/abs/10.1029/2019JD030724`.

[15] J.D. Ingle and S.R. Crouch. *Spectrochemical Analysis*. Prentice Hall, 1988. ISBN 9780138268763.

[16] John Monteith and Mike Unsworth. *Principles of Environmental Physics*. Academic Press, 2017. ISBN 978-0-080-92479-3.

[17] Shaoul Ezekiel. Laser Fundamentals II. `https://ocw.mit.edu/courses/res-6-005-understanding-lasers-and-fiberoptics-spring-2008/resources/laser-fundamentals-ii/`, 2008. [Accessed: 17.06.2022].

[18] Hans Joachim Eichler, Jürgen Eichler, and Oliver Lux. *Lasers*. Springer International Publishing, 2018. ISBN 978-3-319-99895-4.

[19] Pradip Narayan Ghosh. *Laser Physics and Spectroscopy*. CRC Press, 2018. ISBN 978-1-138-58827-1.

[20] H. Kogelnik and T. Li. Laser beams and resonators. *Appl. Opt.*, 5(10):1550–1567, Oct 1966. doi: 10.1364/AO.5.001550. URL http://opg.optica.org/ao/abstract.cfm?URI=ao-5-10-1550.

[21] Melles Griat. Gaussian Beam Optics. http://experimentationlab.berkeley.edu/sites/default/files/MOT/Gaussian-Beam-Optics.pdf, 2022. [Accessed: 27.06.2022].

[22] ISO 11146. Lasers and laser-related equipment - Test methods for laser beam widths, divergence angles and beam propagation ratios. https://www.iso.org/standard/77769.html, 2021. [Accessed: 05.07.2022].

[23] Coherent. Obis lx 637 nm laser system. https://coherentinc.force.com/Coherent/1412450?cclcl=en_US, 2022. [Accessed: 05.07.2022].

[24] Toptica. Continuously Tunable Laser (CTL). https://www.toptica.com/products/tunable-diode-lasers/ecdl-dfb-lasers/ctl/, 2022. [Accessed: 05.07.2022].

[25] Ekspla. Nt340 series, high energy broadly tunable lasers. https://ekspla.com/product/nt340-series-tunable-lasers/, 2022. [Accessed: 05.07.2022].

[26] Guido Van Rossum and Fred L. Drake. *Python 3 Reference Manual*. CreateSpace, Scotts Valley, CA, 2009. ISBN 1441412697.

[27] Annika Oetjens. Github: Laser beam propagation. https://github.com/oetjensa/laser_ABCD, 2022. [Accessed: 05.07.2022].

[28] MRC Systems. Active laser beam stabilization. https://www.mrc-systems.de/en/products/laser-beam-stabilization, 2022. [Accessed: 05.07.2022].

Erklärung

Ich versichere, dass ich diese Arbeit selbstständig verfasst habe und keine anderen als die angegebenen Quellen und Hilfsmittel benutzt habe.

Heidelberg, den 8. Juli 2022